Experimental and Theoretical Electron Density Analysis of Copper Pyrazine Nitrate Quasi-Low-Dimensional Quantum Magnets

Leonardo H. R. Dos Santos,[†] Arianna Lanza,[†] Alyssa M. Barton,[‡] Jamie Brambleby,[+] William J. A. Blackmore,[+] Paul A. Goddard,[+] Fan Xiao,[⊥] Robert C. Williams,[⊥] Tom Lancaster,[⊥] Francis L. Pratt,[#] Stephen J. Blundell,[§] John Singleton,[◊] Jamie L. Manson*[,‡] and Piero Macchi*[,†]

[†] Department of Chemistry and Biochemistry, University of Bern, Freiestrasse 3, 3012 Bern, Switzerland

[‡] Department of Chemistry and Biochemistry, Eastern Washington University, 226 Science, Cheney, WA 99004, United States

[+] Department of Physics, University of Warwick, Gibbet Hill Road, Coventry, CV4 7AL, United Kingdom

[⊥] Department of Physics, Durham University, South Road, Durham, DH1 3LE, United Kingdom

[#] ISIS Facility, STFC Rutherford Appleton Laboratory, Chilton, Oxon OX11 0QX, United Kingdom

[§] Clarendon Laboratory, Department of Physics, University of Oxford, Oxford OX1 3PU, United Kingdom

[◊] National High Magnetic Field Laboratory, Los Alamos National Laboratory, Los Alamos, NM 87545, United States

ABSTRACT: The accurate electron density distribution and magnetic properties of two metal-organic polymeric magnets, the quasi-one-dimensional (1D) $Cu(pyz)(NO_3)_2$ and the quasi-two-dimensional (2D) $[Cu(pyz)_2(NO_3)]NO_3{\cdot}H_2O$, have been investigated by high-resolution single-crystal X-ray diffraction and Density Functional Theory calculations on the whole periodic systems and on selected fragments. Topological analyses, based on Quantum Theory of Atoms in Molecules, enabled the characterization of possible magnetic exchange pathways and the establishment of relationships between the electron (charge and spin) densities and the exchange-coupling constants. In both compounds, the experimentally observed antiferromagnetic coupling can be quantitatively explained by the Cu-Cu superexchange pathway mediated by the pyrazine bridging ligands, via a σ-type interaction. From topological analyses of experimental charge-density data, we show for the first time that the pyrazine tilt angle does not play a role in determining the strength of the magnetic interaction. Taken in combination with molecular orbital analysis and spin density calculations, we find a synergistic relationship between spin delocalization and spin polarization mechanisms and that both determine the bulk magnetic behavior of these Cu(II)-pyz coordination polymers.

INTRODUCTION

Magnetic materials find use in telecommunications, information storage, thermomagnetic heat transfer, electrical-to-mechanical power conversion, catalysis, magnetic separation and countless other fields.[1] Research in this area involves engineering and synthesis of materials exhibiting preconceived magnetic behavior, often based on a relative understanding of quantum-mechanical phenomena.[2] Of particular appeal are coordination polymers, where the magnetic centers are typically metal ions, and the metal-organic or organometallic building blocks are connected through covalent bonds, coordination interactions and weaker intermolecular bonds.[3] The interplay between chemical interactions of different strength may lead to single-molecule behaviors (*e.g.*, low-spin-high-spin transitions), low-dimensional properties (as observed for magnetic chain compounds) or three-dimensional long-range ordering (*e.g.*, ferromagnetic crystals). Most of the magnetic coupling models applied to molecular-based systems[4] rely on (super)exchange interactions between two paramagnetic centers, whose atomic wavefunctions overlap. For systems with large metal-metal separation, like in ligand-bridged polymetallic systems, no direct bonding can take place between the two metals and the magnetic interactions are mediated by diamagnetic, ideally closed-shell ligands, acting as couplers, rather than as mere spacers. Therefore, the understanding of magnetic coupling mechanisms, as required to design new materials with enhanced properties, relies intimately on the strength and nature of intra- and intermolecular interactions.

The variety of structural and magnetic data available for polynuclear transition-metal complexes has established important structure-property relationships.[3b,5] Nevertheless, the prediction of their magnetic behavior is far from trivial, mainly due to the intricate interplay between different factors that determine the exchange processes. From this perspective, the knowledge of the electronic structure of polymetallic systems is of particular importance, given that the spin density determines the sign and magnitude of the exchange-coupling constants.[6] Among the experimental techniques available to determine electronic spin density distributions, single-crystal polarized neutron diffraction (PND) stands apart because it affords enormous possibilities to understand the magnetic mechanisms at the atomic and molecular levels. It allows reconstruction of the periodic spin density by fitting either a set of atomic wavefunctions or a multipolar model at various levels of sophistication.[7] Furthermore, the reconstruction of spin-resolved electron densities is possible nowadays by combining polarized neutron and high-resolution X-ray diffractions.[8] From the theoretical side, reasonable estimates of the exchange-coupling constants can be found for very large or even periodic systems thanks to density functional theory (DFT).[9] These studies are crucial because the interpretation of experimental measurements at the atomic and molecular level is not trivial, especially for systems containing many paramagnetic centers. In such cases, theoretical spin densities and orbital analyses have been demonstrated to be very important.[10]

In recent years, the determination and analysis of the position electron-densities alone, either theoretical or experimental, played an important role in advancing chemical bonding theory, which directly impacts our understanding of superexchange mechanisms.[11]

Among magnetic coordination polymers, quasi-1D or -2D compounds are of particular interest because they are intermediate situations between high-nuclearity magnetic clusters and three-dimensional magnetic frameworks.[4] These compounds are characterized by ordered chains or layers consisting of metal ions bridged by polydentate ligands. These architectures lead to predominantly low-dimensional ferromagnetic (FM) or antiferromagnetic (AFM) materials, even though weak interchain and interlayer couplings can also take place, giving rise to three-dimensional pathways and sometimes magnetic ordering, depending on the molecular structure and crystal packing.[12] Furthermore, 1D magnets have long been recognized as prototypical for the experimental studies of physics in reduced dimensions, with the linear chain Heisenberg antiferromagnet model (LCHAFM) being the subject of extensive investigations.[4] Quasi-1D Cu-compounds are widely studied,[13] but copper(II) pyrazine dinitrate, $Cu(pyz)(NO_3)_2$ (**1**), has been the most successful realization of the LCHAFM. This material has a relatively small exchange-coupling constant, J = –7.26 cm^{-1} (–10.4 K), as determined from magnetic susceptibility, high-field magnetization, specific heat measurements and inelastic neutron scattering.[14a] The ratio of interchain to intrachain exchange constants, J'/J, has been estimated to be negligible, implying that the chains can be considered as isolated. However, evidence for three-dimensional long-range magnetic order has been recently detected below 0.107 K based on zero-field muon-spin relaxation measurements.[14b] This technique provided an estimation of J'/J significantly larger than previously expected, although J' = +0.03 cm^{-1} (+0.046 K) is still very small.[14b] An ordered magnetic moment of ~0.05 μ_B was also established, a value extremely difficult to confirm via other experimental means. On the other hand, the cationic three-dimensional net of copper(II) di(pyrazine) nitrate, $[Cu(pyz)_2(NO_3)]^+$, is investigated here for the first time, as obtained in single-crystals of the hydrated coordination polymer $[Cu(pyz)_2(NO_3)]NO_3{\cdot}H_2O$ (**2**).

In this work, we correlate the accurate electron density distributions in **1** and **2** with their magnetic properties. For **1**, both the experimental density (from X-ray diffraction) and theoretical density (from quantum-mechanical calculations) are investigated. For **2**, only theoretical electron densities are discussed because single-crystals suitable for accurate high-resolution X-ray diffraction experiments could not be obtained. Difficulties abound to determine the experimental spin densities of **1** or **2** using PND: (a) growth of suitably-sized single crystals, (b) adequate magnetic field strength to overcome AFM couplings, i.e., induce the fully polarized state, and (c) presence of quantum fluctuations that leads to a small Cu(II) ordered moment.

Quantitative reasoning of the chemical bonding, in particular around the metallic center, is achieved using the real-space partitioning derived from quantum theory of atoms in molecules (QTAIM). This study is particularly devoted to establishing relationships between the electron charge and spin densities and the exchange-coupling constants. Our investigation is supplemented by molecular orbital analyses. From this work, we also reveal the cooperative nature of spin delocalization and spin polarization mechanisms and that they are not mutually exclusive. This finding may be representative of the larger class of copper(II) pyrazine quantum magnets.

EXPERIMENTAL SECTION

Synthesis. Purple needle-shaped single-crystals of **1** were grown from aqueous mixtures of $Cu(NO_3)_2{\cdot}3H_2O$ and 1 eq. of pyrazine. Deep blue plates of **2** were prepared from aqueous mixtures containing a large excess of pyrazine (12.6 eq.).

X-ray Data Collection and Structure Refinement. Single-crystals of **1** and **2** were mounted on an Agilent SuperNova diffractometer. The crystals were cooled to 100 K (**1**) and 173 K (**2**) with N_2. The *CrysAlisPro* programs were used to perform data collection and reduction.[15] A total of 24441 and 12729 intensities were harvested, respectively for **1** and **2**. Numerical absorption corrections were applied. The resulting data for **1** was additionally sorted and merged in Laue group *mmm* using SORTAV,[16] giving 2933 independent reflections with a mean redundancy of 8.3 and up to a resolution of $sin\theta_{max}/\lambda = 1.19$ Å^{-1}. Additional data are tabulated in Table 1. Coordinates and atomic displacement parameters (ADPs) were refined applying the independent-atom model (IAM) as implemented in SHELXL.[17] The experimental geometries are shown in Figure 1. No single crystal sample of species **2** was found with a sufficient quality for an electron density study. In fact, peak broadening was always observed at high diffraction angle, caused by unavoidable defects during the crystal growth, despite several crystallizations, in different conditions, were attempted.

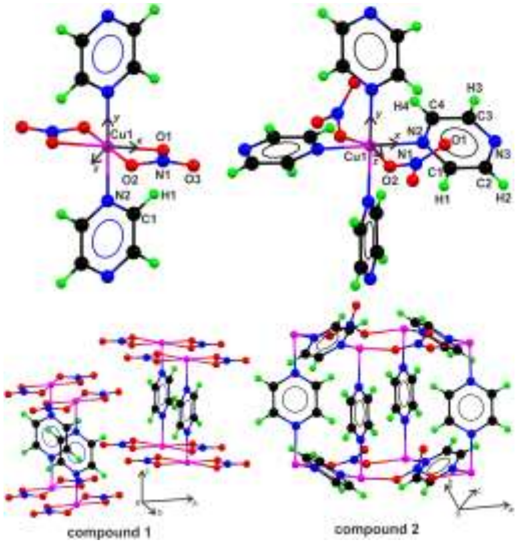

Figure 1. Experimental structure of crystalline $Cu(pyz)(NO_3)_2$ (**1**) and $[Cu(pyz)_2(NO_3)]NO_3{\cdot}H_2O$ (**2**). Only the asymmetric units are labelled. Local axes at the copper atoms are also shown. For **2**, counter-ions and solvent molecules are omitted.

Multipole Refinement. The IAM parameters were used as initial values for multipole modelling of **1**. This was performed using the XD2006 program[18] and the Hansen-Coppens formalism. A number of models were tested to optimize the fit to the experimental intensities. In the final model, the multipole expansion was truncated at the hexadecapole level for all the non-H atoms, while only a bond-directed dipole was applied to H1. The κ parameters were refined for each atomic type. For O, N and C atoms, a single κ_l' was refined for all the l values belonging to a defined set while κ_l' for Cu and H1 were constrained to the corresponding refined κ values. A high-order refinement with $\sin\theta/\lambda \geq 0.7$ Å^{-1} was performed for the non-hydrogen atoms to obtain accurate positional and displacement parameters. Afterwards, the H-atom coordinates and isotropic ADP were freely refined. An isotropic extinction coefficient was also refined according to the Becker-Coppens equations.[19]

Table 1. Crystallographic Details and Refinement Results for Compounds **1** and **2**

Crystal data	Cu(pyz)$(NO_3)_2$ (**1**)	[Cu$(pyz)_2(NO_3)$]$NO_3.H_2O$ (**2**)
Chemical formula	$CuC_4H_4N_4O_6$	$(CuC_8H_8N_5O_3)NO_3.H_2O$
Crystal system, space group	Orthorhombic, *Pmna*	Orthorhombic, *Ima2*
Temperature (K)	100.0 (5)	173.0 (5)
a, *b*, *c* (Å)	6.70122 (7), 5.11854 (5), 11.6351 (1)	13.6081 (5), 9.9487 (4), 9.4287 (3)
V (Å^3)	399.089 (7)	1276.48 (8)
Z	2	4
μ (mm^{-1})	2.757	1.762
Crystal size (mm^3)	0.22 × 0.12 × 0.08	0.07 × 0.07 × 0.03
Data collection		
No. of measured, independent and observed [$F > 3\sigma(F)$] reflections	24441, 2933, 2737	12729, 1821, 1503
R_{int} [a]	0.018	0.083
$(\sin\theta/\lambda)_{\max}$ (Å^{-1})	1.188	0.697
Independent-atom model refinement		
Refinement on	F^2 (for $F > 0$)	F^2 (for $F > 0$)
$R[F > 3\sigma(F)]$, R_{all}, wR, S [b]	1.68, 1.92, 2.67, 1.39	5.11, 7.95, 6.08, 1.14
No. of parameters	48	113
$\Delta\rho_{\max}$, $\Delta\rho_{\min}$ (e Å^{-3})	0.53, −1.22	0.94, −0.92
Extinction coefficient	0.023 (2)	
Multipole refinement		
Refinement on	F^2 (for $F > 0$)	
$R[F > 3\sigma(F)]$, R_{all}, wR, S [b]	0.95, 1.18, 1.40, 0.83	
No. of parameters	175	
$\Delta\rho_{\max}$, $\Delta\rho_{\min}$ (e Å^{-3})	0.28, −0.22	
Extinction coefficient	0.045 (2)	

[a] $R_{int} = \sum_{\boldsymbol{h}} \left| F^2_{\boldsymbol{h},obs} - \langle F^2_{\boldsymbol{h},obs} \rangle \right| / \sum_{\boldsymbol{h}} F^2_{\boldsymbol{h},obs}$ (summation is carried out only where more than one symmetry equivalent reflection is averaged).

[b] $R(F) = 100.\sum_{\boldsymbol{h}} \left| |F_{\boldsymbol{h},obs}| - |F_{\boldsymbol{h},calc}| \right| / \sum_{\boldsymbol{h}} |F_{\boldsymbol{h},obs}|$, $wR(F) = 100.\left[\sum_{\boldsymbol{h}} w_{\boldsymbol{h}} \left(|F_{\boldsymbol{h},obs}| - |F_{\boldsymbol{h},calc}| \right)^2 / \sum_{\boldsymbol{h}} w_{\boldsymbol{h}} F^2_{\boldsymbol{h},obs}\right]^{1/2}$, $S = \left[\sum_{\boldsymbol{h}} w_{\boldsymbol{h}} \left(F^2_{\boldsymbol{h},obs} - F^2_{\boldsymbol{h},calc} \right)^2 / (N-P)\right]^{1/2}$ with $w_{\boldsymbol{h}} = 1/\sigma^2_{\boldsymbol{h},obs}$, N is the number of reflections and P is the number of parameters.

The ground-state electronic configuration of Cu corresponds to [Ar]$4s^1 3d^{10}$ and the 4s orbital is well known to contribute to the valence density. However, it is also established that transition metals present problems when refining the deformation density because of the significantly different radial extensions of the (n-1)d and ns valence orbitals. This would require the treatment of two different valence deformation densities or, as it is often the case, that the ns density is constrained to its nominal value and formally associated with the frozen core density.[20] In **1**, scattering from the copper 4s density is only significant for $\sin\theta/\lambda < {\sim}0.18$ Å^{-1} and only 14 reflections satisfy this criterion. In view of such a small number of reflections, their standard uncertainty and the fact that P_{00} is expected to be a rather small quantity, it is not surprising that attempts to refine the 4s population independently through the $l = 0$ deformation function gave physically unrealistic populations. Thus, a model based on the [Ar]$4s^0 3d^9$ electronic distribution for Cu(II) was also tested. This gave significantly better residuals and the final model was based on this configuration.

Anharmonic motion[21] was modelled for the Cu atom by refining Gram-Charlier coefficients up to fourth-order. It led to an improvement on the residual density distribution in the vicinity of the Cu nucleus. The probability density function (p.d.f.) for this atom can be found in the Supporting Information.

In the final refinement, the maximum and minimum residual density peaks were +0.29 and –0.22 $e.\text{Å}^{-3}$ using all data. Residual density maps show only few and small discrepancies that could not be removed by any deformation model (see Supporting Information).

Topological properties and integrated atomic charges were calculated using the TOPXD module.[18] Recent studies suggest an estimate of approximately ±5% for the accuracy of the integrated atomic properties.[22]

Static Magnetization Measurements. The temperature-dependence of the magnetization for **1** and **2** were measured using a Quantum Design MPMS 7 T SQUID magnetometer. Polycrystalline samples were coated in high vacuum grease, loaded into a gelatin capsule, mounted in a plastic drinking straw, and affixed to the end of a stainless steel/brass rod. Sample rods were loaded into the SQUID at room temperature and cooled in zero-field to a base temperature of 1.8 K. At that temperature, the magnetic field was charged to 0.1 T and data collected upon warming back to 300 K. All magnetic data were corrected for core diamagnetism using values typical of the constituent atoms.

Pulsed-field magnetization. The pulsed-field magnetization experiments (up to 60 T) used a 1.5 mm bore, 1.5 mm long, 1500-turn compensated-coil susceptometer, constructed from 50-gauge high-purity copper wire.[23] When a sample is placed within the coil, the signal voltage *V* is proportional to (d*M*/d*t*), where *t* is the time. Numerical integration of *V* is used to evaluate *M*. The sample is mounted within a 1.3 mm diameter ampule that can be moved in and out of the coil. Accurate values of *M* were obtained by subtracting empty coil data from that measured under identical conditions with the sample present. The susceptometer was placed inside a ^{3}He cryostat providing temperatures down to 0.5 K. The field *H* was measured by integrating the voltage induced in a ten-turn coil calibrated by observing the de Haas−van Alphen oscillations of the belly orbits of the copper coils of the susceptometer.

Muon-spin relaxation. Zero-field μ^+SR measurements on **2** were carried out on a powder sample using the EMU spectrometer at the ISIS facility, UK. The sample was packed in an Ag envelope (foil thickness 25 μm) and mounted on an Ag backing plate using vacuum grease and loaded inside a ^{4}He cryostat.

Theoretical Calculations. The exchange-coupling constant *J* can be related to the energy difference between states with different spin multiplicities.[24] For this purpose, accurate unrestricted wavefunctions for the high- and low-spin states are required. However, because accurate calculations on the low-spin state are not straightforward, a broken-symmetry solution is usually assumed as a good approximation to the wavefunction of this state. We have investigated the high-spin and the broken-symmetry states in the dinuclear molecular models of compounds **1** and **2**, represented in Figure 2. Models 1-d1 and 2-d1 comprise dimeric versions of the infinite chain structures present in **1** and **2** respectively. They contain two Cu centers bridged by a pyrazine ligand, while the other models account for interchain interactions or intrachain pathways mediated by the nitrate ligand. All systems have been investigated within unrestricted Kohn-Shan approximation using the B3LYP/6-311G(2d,2p) level of theory, as implemented in the Gaussian 09 package.[25] The AIMAll software[26] has been used to partition the corresponding electron densities and to calculate integrated atomic properties.

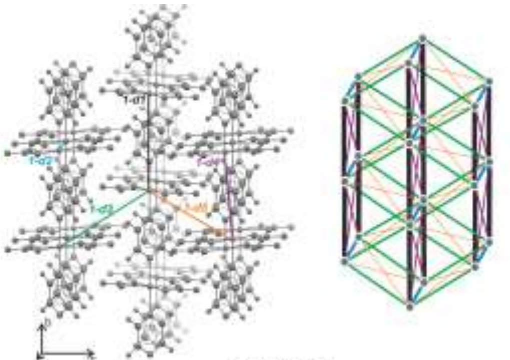

compound 1

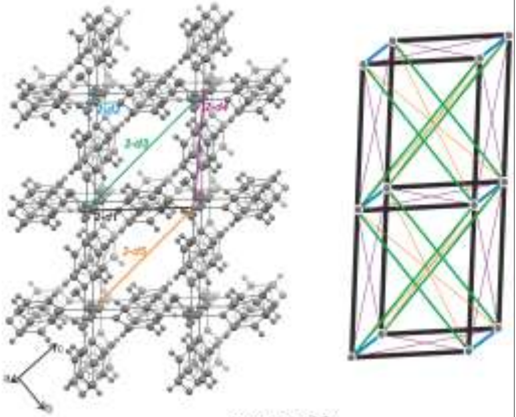

compound 2

Figure 2. Disposition of the dinuclear models in $Cu(pyz)(NO_3)_2$ (**1**) and $[Cu(pyz)_2(NO_3)]NO_3{\cdot}H_2O$ (**2**). Schematic views of the packing in terms of Cu positions and the network generated from the shortest Cu···Cu contacts are also shown with line thickness representing the relative magnitude of the coupling constants.

The CRYSTAL09 code[27] was used to perform periodic DFT calculations on relevant ferro- and antiferromagnetic phases of **1** and **2** using the B3LYP hybrid functional. The basis set for the Cu atom is 86-411G(41d),[28] while for the non-metallic atoms, it is 6-31G(1d).[29] Topological analysis of the periodic electron densities and integrated atomic properties were calculated using the TOPOND09 software.[30]

Our periodic calculations on **1** considered the magnetic phases schematically represented in Figure 3. The ferromagnetic phase (FM) corresponds to the high-spin structure, whereas the antiferromagnetic phases (AFM) correspond to low-spin ones. The unit cell of FM and sAFM contain two formula units whereas the simulations of the aAFM and the bAFM phases require double cells. Due to prohibitively high computational costs, only the phases FM and sAFM were investigated for compound **2**, see Figure 3. The coupling constant can be estimated from the energy gap between the FM phase and the AFM phase according to well established protocols.[31] To obtain a fair comparison with experiment, the calculated structure factors of the FM and AFM phases of **1** were fitted against the best multipolar model derived experimentally.

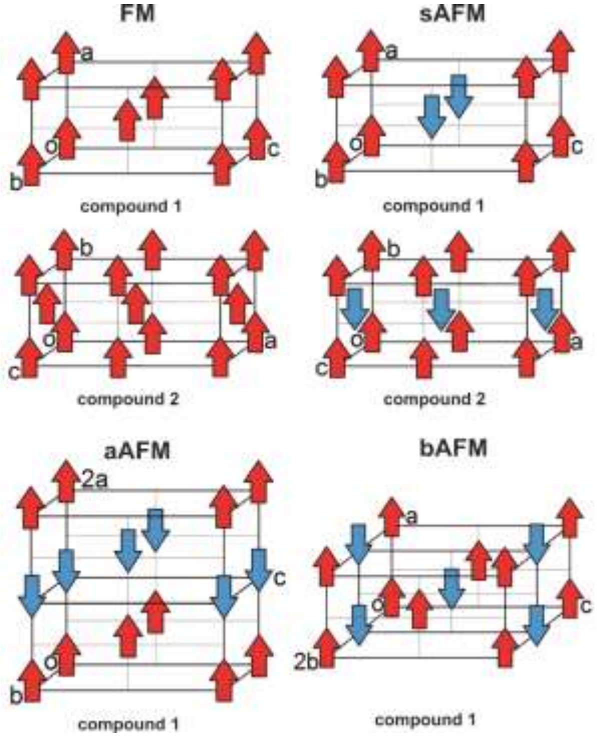

Figure 3. Orthorhombic unit cells for magnetic phases of $Cu(pyz)(NO_3)_2$ (**1**) and $[Cu(pyz)_2(NO_3)]NO_3{\cdot}H_2O$ (**2**). The ferromagnetic (FM) and three possible antiferromagnetic (sAFM, aAFM and bAFM) structures are considered. Red and blue arrows indicate Cu(II) moments.

RESULTS AND DISCUSSION

Structural investigations carried out on molecular magnetic materials enable a tentative correlation of the exchange-coupling constant *J* with geometrical parameters, in particular for spin-only or dinuclear systems.[32] Intermetallic distances or angles between metal centers and bridging ligands are often considered representative of orbital overlap for an intuitive understanding of the (super)exchange mechanism.[3] However, only a few studies have been carried out to correlate the magnetic behavior of a material with its electron density distribution, as experimentally obtained from high-resolution X-ray diffraction.[11]

We briefly describe the crystal structures of **1** and **2**, then we analyse their electron density, either obtained experimentally (**1**) or theoretically (**1** and **2**). Finally, we complement our study through molecular orbital analysis of the spin-density distributions, and magnetic responses measured for **1** and **2**.

Crystal Structures. Our charge density data collection on $Cu(pyz)(NO_3)_2$ 1D polymer implied also a re-determination of the structure (Figure 1), without any major difference with previous studies.[14a,33] Each Cu occupies a 2/*m* crystallographic site and lies at the center of a distorted octahedron formed by two of each Cu–O1 [2.0022 (2) Å], Cu–O2 [2.4796 (3) Å] and Cu–N2 [1.9765 (2) Å] chemical bonds. Adjacent metallic centers are linked by pyrazines along the crystallographic *a* direction, whereas the nitrates lie at the 0, *y*, *z* and ½, *y*, *z* mirror planes. Owing to the symmetry of Cu, all N2–Cu–O angles are 90°, whereas the O1–Cu–O2 angle of 56.74 (2)° is far from the ideal octahedral angle, due to the inherent rigidity of the nitrate ligand. Along the Cu-pyrazine chain, the Cu atoms are separated by 6.701 (1) Å. Weak C–H···O hydrogen bonds [C1···O2 = 3.447 (1) Å] and C···O contacts [C1···O3 = 3.122 (1) Å] connect adjacent chains along the *b* direction. As discussed in the following, although these interactions may stabilize the three-dimensional lattice, our results confirm the weak nature of the superexchange pathways. Thus, the material would be regarded as a 1D quantum magnet.

The crystal structure of the 3D $[Cu(pyz)_2(NO_3)]NO_3{\cdot}H_2O$ coordination polymer was determined here for the first time (Figure 1). The presence of two pyrazine ligands per Cu induces a 3D coordinative network, given that each ligand acts as a bidentate bridge. The cavities formed by the $[Cu(pyz)_2(NO_3)]^+$ network are filled by a non-coordinating nitrate and a water molecule. The Cu(II) ion lies on a 2-fold axis, at the center of a slightly distorted octahedron formed by two of each Cu–O2 [2.337 (4) Å], Cu–N2 [2.039 (9) Å] and Cu–N3 [2.038 (9) Å] bonds. The N2–Cu–N3 angle is almost right [88.8 (1)°], whereas O2–Cu–N3 and O2–Cu–N2 are more distorted [83.8 (2)° and 95.3 (2)°, respectively]. The pseudo-tetragonal Cu-pyrazine layers lie perpendicular to the *a*-direction and the Cu-pyz-Cu edges expand along the {011} and {01-1} directions, with Cu···Cu distances of 6.853 (5) Å. The NO_3^- ligands connect the layers [Cu···Cu = 6.804 (2) Å] along the pseudo Jahn-Teller distorted direction. Thus, the relevant super-exchange pathways are those bridged by pyrazines, addressing the material as a 2D quantum magnet.

Electron Density Distributions and Topological Analysis. In the following, we will discuss results from both the experimental and the theoretical determination of the electron density. Formally, Cu has oxidation state +2 in both **1** and **2**. Being a d^9 metal, the observed stereochemistry can be explained by *pseudo*-Jahn-Teller distortion, *i.e.* the stabilization of four coordination directions in a plane and the destabilization of the two remaining out of the plane directions. The analysis of the electron density distribution enables investigating in details these features, going beyond the mere bond lengths. The electron population of Cu reflects the bonding mechanism of the ligand-to-metal electron donation and the potential metal-to-ligand back donation. The electron distribution around Cu also informs on the specific bonding contribution, identifies the magnetic orbital and provides more details of the Jahn-Teller distortion.

The experimentally refined valence population of Cu in **1** is 9.89 (8) *e*. The multipolar expansion is itself an atomic partitioning, hence the valence monopole population determines the atomic charge, here +1.11(8) *e* for **1**. However, because the multipolar parameters correlate within a refinement (the largest correlation coefficients among different atoms in the multipolar refinement of **1** are ca. 40%) and different combinations of multipolar coefficients may describe the same electron density distribution, a better estimation of the atomic charges comes from a partitioning of the total density reconstructed from the multipolar model. QTAIM offers a more exportable method of determining atomic charges and it enables an unbiased comparison between theoretical and experimental electron density. In Table 2, charges are shown for the experimental multipolar fitted density of **1**, and for the periodically calculated FM and AFM densities, and the calculated dinuclear model densities of **1** and **2**. Charges from Hirshfeld partitioning are reported in the Supporting Information.

Table 2. Experimental and Theoretical QTAIM Charges on Relevant Atoms and Ligands of Compounds **1** and **2**[a]

	Cu(pyz)(NO$_3$)$_2$ (**1**)				[Cu(pyz)$_2$(NO$_3$)]NO$_3$.H$_2$O (**2**)	
	MM Exptl.	MM FM/AFM	FM/AFM	Dinuclear Models	FM/AFM	Dinuclear Models
Cu	+1.08	+1.44	+1.27	+1.19	+1.25	+1.22
O1	-0.47	-0.44	-0.61	-0.61		
O2	-0.53	-0.52	-0.57	-0.54	-0.61	-0.49
N2	-1.20	-0.85	-1.33	-1.14	-1.29	-1.07
N3					-1.30	-0.93
pyrazine	+0.44	-0.06	+0.38	+0.24	+0.29	+0.20
nitrate	-0.72	-0.68	-0.82	-0.72	-0.91	-0.85

[a] MM Exptl.: $\rho(\mathbf{r})$ from the multipole model fitted against the experimental structure factors; MM FM/AFM: $\rho(\mathbf{r})$ from the multipole model fitted against the periodic-B3LYP structure factors; FM/AFM: $\rho(\mathbf{r})$ directly from the periodic-B3LYP calculation; Dinuclear models: $\rho(\mathbf{r})$ from the gas phase B3LYP calculation.

Despite their inherent differences, all partitioning schemes, applied to experimental and theoretical electron densities, indicate that Cu(II) receives quite substantial donation from the ligands, thus reducing its formal charge. In fact, pyrazine features a slightly positive charge and the nitrate is largely negative, but less than -1. All atoms that bind Cu bear rather negative charges.

Beside the charges, the electron distribution around the atoms is useful to identify the features affecting the magnetism of the systems. Experimental deformation density maps around Cu(II) (shown in Figure 4 for **1**) address a significant electron density depletion in the copper valence shell towards the directions defining the $3d_{x^2-y^2}$ orbital. They correspond to the Cu–O1 and Cu–N2 bond directions for **1** and to the two Cu–pyrazine directions for **2**, in keeping with the expectations from bond distances. Complementarily, the electron density on the ligand binding atoms is accumulated in these directions. More interesting is analysing the charge density along the Jahn-Teller distorted directions (Cu-O2, for both **1** and **2**). Of course, Cu presents a charge accumulation along its z axis (due to the $3d_{z^2}$ orbital) that would produce a repulsion with the O2 lone pair lobe. However, in **1** (and somewhat in **2** as well), the lone pair on O2 tends to minimize the destabilizing interaction with $3d_{z^2}$ and partially interact also with the depletion of $3d_{x^2-y^2}$. The Laplacian maps (see Supporting Information) fully confirm this evidence, as well as the bond path shapes (see below).

The topological analysis of $\rho(\mathbf{r})$ (Table 3 for the main chemical bonds in **1**; Supporting Information for **2**) is also very useful to clarify the nature of the interactions. First, we have to stress that in the theoretical electron densities there is no appreciable difference as a function of the spin coupling mechanisms (FM or AFM phases). Therefore, results of the topological analysis of the periodic DFT calculations are collectively tabulated under the heading FM/AFM. The models calculated for dinuclear clusters (Figure 2) give only slightly different values and overall, there is a close agreement between the theoretical and the experimental results for **1**. As expected,[34] the electron density at the bond critical points ρ_{bcp} closely correlates with the Cu–X distances. For both **1** and **2**, it is easy differentiating the bonds along the pseudo Jahn-Teller distortion (z) from those in the xy plane: Cu–O2 is associated with a much smaller amount of electron density and a rather flat region. All the coordinative interactions at Cu are characterized by positive Laplacian at the bond critical points ($\nabla^2\rho_{bcp}$). This is not surprising and, at variance with what is sometimes stated in the literature, it does not indicate any predominance of closed-shell character.[34b] In fact, the delocalization index[35] (DI, available only from theoretical density) of all Cu–X bonds is approximately one-half of an electron pair, except for Cu–O2 (DI ca. 0.1) in keeping with the smaller ρ_{bcp} and $\nabla^2\rho_{bcp}$. The Cu–O2 bond path in **1** is significantly bent (Figure 4) towards the magnetic orbital $d_{x^2-y^2}$, indicating that the Cu–O2 interaction partially involves this orbital whereas no interaction with d_{z^2} occurs. Albeit smaller, a similar bending characterizes the corresponding bond-path in **2**, where no stereochemical constraint forces O2 to deviate from z direction. As a consequence of the curvature, the ellipticity of Cu–O2 is considerably larger than for the other Cu–X bonds.

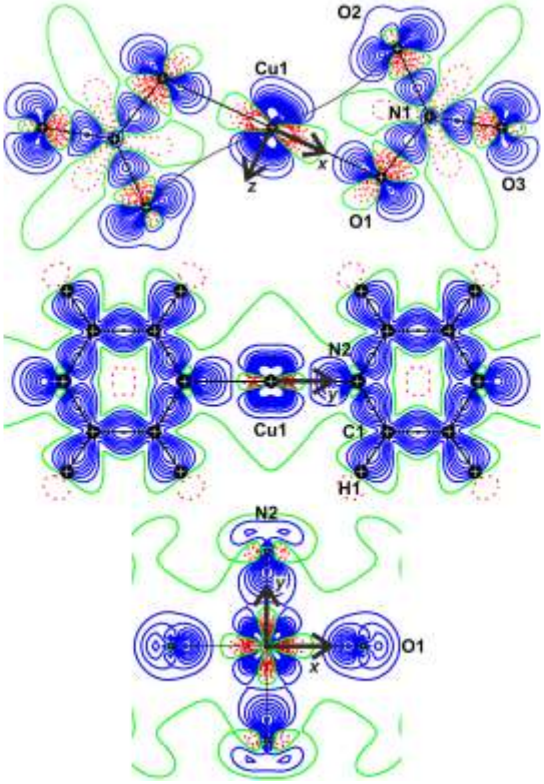

Figure 4. Experimental static deformation densities for Cu(pyz)$(NO_3)_2$ (**1**). Positive contours as solid blue lines, negative contours as dotted red lines and zero contours as solid green lines. The contour level is 0.015 au.

The atomic graph of Cu (obtained from the topology of $L(\mathbf{r}) = -\nabla^2\rho(\mathbf{r})$) is quite informative of its stereochemistry. For **1**, both the experimental (Figure 5) and the periodic DFT calculations (Supporting Information) speak for a rather distorted octahedral coordination. The emerging graph is in keeping with the expectations of the ligand field theory: the 3d electrons avoid the charge concentrations of the ligands. In the Cu VSCC region, critical points of $L(\mathbf{r})$ are located *ca*. 0.28 – 0.30 Å from the nucleus, being mainly determined by the 3d electronic shell. The six (3,+1) critical points (charge depletions) are along the 4-fold axes of the ideal octahedron, thus in direction of the ligand atoms; the four (3,–3) critical points represent charge concentrations in the *xy* plane, whereas eight (3,–1) critical points are found out of this plane. In the region of valence shell charge depletion (VSCD), six (3,+3) critical points are found along the six bond paths emanating from the metallic center and approximately at 0.42 Å from the nucleus. This topology can be compared with that of a Cu^{2+} in a perfectly octahedral environment (calculated by imposing an O_h-field splitting of the d orbitals). The graph of this Jahn-Teller unstable configuration would have the topology of a cube, see Figure 5. Upon distortion along z, the (3,–3) critical points lying on the vertexes of the cube collapse onto the *xy* plane defined by the d_{xy} orbital. Along z, the (3, –1) charge accumulations remain, two of them would be in proximity of the VSCC of O2. Because of the repulsion between Cu (3, –1) and O2 (3, –3) charge concentrations, the former critical points assume a distorted topology respect to that observed in an O_h field: the (3, –1) points in the *xz* plane are closer to the (3,+1) in **1**, while the corresponding points in the *yz* plane are farther from the (3,+1) points. However, the distance of the (3, –1) critical points to the Cu remains constant (0.28 Å). Moreover, the repulsion between the Cu (3, –1) and O2 (3, –3) charge concentrations also causes the observed bending of the Cu–O2 bond-path. This means that the weak Lewis acidity of the Cu(II) in *z* direction is not used by the second coordination of the nitrate that prefers instead using the stronger Lewis acidity of the magnetic orbital. Although smaller, this effect also occurs in **2**, where the atomic graph of Cu is a cuboid elongated in the *z* direction, as a consequence of the pseudo-tetragonal symmetry of the Cu$(pyz)_2$ layers.

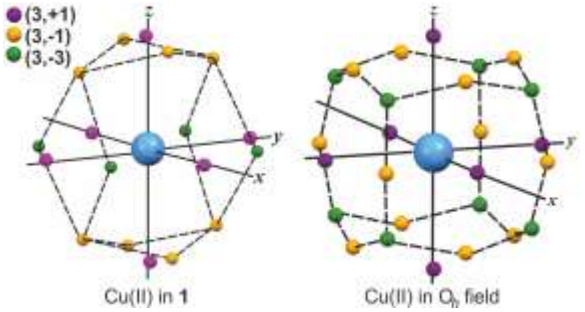

Figure 5. Atomic graph of Cu obtained experimentally in Cu(pyz)$(NO_3)_2$ (**1**) and calculated in a octahedral environment.

Table 3. Selected Bond Critical Point Properties for Cu(pyz)$(NO_3)_2$ (**1**)[a]

		MM Exptl.	MM FM/AFM phases	FM/AFM phases	Dinuclear models
Cu–O1	d_{bcp}	0.990	0.998	0.965	0.966
	ρ_{bcp}	0.068	0.082	0.075	0.074
	$\nabla^2\rho_{bcp}$	0.425	0.377	0.447	0.386
	ϵ	0.24	0.31	0.10	0.09
	DI				0.410
Cu–O2	d_{bcp}	1.237	1.269	1.223	1.235
	ρ_{bcp}	0.023	0.034	0.027	0.028
	$\nabla^2\rho_{bcp}$	0.119	0.108	0.096	0.109
	ϵ	1.07	0.75	0.84	0.54
	DI				0.111
Cu–N2	d_{bcp}	0.952	0.974	0.907	0.943
	ρ_{bcp}	0.094	00123	0.111	0.090
	$\nabla^2\rho_{bcp}$	0.445	0.416	0.604	0.417
	ϵ	0.13	0.10	0.05	0.05
	DI				0.444

[a] d_{bcp} represents the distance, in Å, of the atom A of the A–B bond to the bond critical point, ρ_{bcp} and $\nabla^2\rho_{bcp}$ are the electron density and its Laplacian, in au., at the bond critical point, ϵ is the dimensionless bond ellipticity and DI is the delocalization index. MM Exptl.: $\rho(\mathbf{r})$ from multipole model fitted against experimental structure factors. MM FM/AFM: $\rho(\mathbf{r})$ from multipole model fitted against theoretical structure factors. FM/AFM: $\rho(\mathbf{r})$ directly from the periodic-B3LYP calculation. Experimental standard uncertainties are omitted as they are usually smaller than 10^{-3} au.

d-Orbital Populations and Magnetic Moment. The 3d orbital populations of Cu can be calculated from the refined multipolar parameters[36] (see Table 4). In both **1** and **2**, the choice of local axes (Figure 1) makes $d_{x^2-y^2}$ the most energetically destabilized orbital, and therefore the least populated. As it often occurs, the multipolar populations exceed the limit of two electrons for the fully occupied orbitals. In fact, the multipole functions are d-like density functions, but they may reflect contributions not only by the metal d-orbitals. Nevertheless, their populations qualitatively agree with the expectations of ligand field theory.[37] Thus, we can use the experimental d-orbital populations to estimate the magnetic moment

μ_S (Table 4), assuming the experimentally derived g-factors. Those results agree with experimental measurements on other complexes of Cu(II) in distorted octahedral environment.[37]

Table 4. 3d Atomic Orbital Populations and Spin-Only Magnetic Moments for the Cu Center in Cu(pyz)(NO$_3$)$_2$ (**1**) and [Cu(pyz)$_2$(NO$_3$)]NO$_3$·H$_2$O (**2**), Obtained After Multipolar Refinement of the Experimental Structure Factors of (**1**), and from the Periodic DFT Calculations

	$d_{x^2-y^2}$	d_{xz}	d_{xy}	d_{yz}	d_{z^2}	μ_S/μ_B
Compound **1**						
Exptl.	1.34(2)	2.10(1)	2.22(1)	2.23(1)	2.00(2)	2.15
FM/AFM	1.55	1.99	1.98	1.98	1.76	1.55
Compound **2**						
FM/AFM	1.43	1.98	1.98	1.98	1.99	1.38

Table 5. Exchange-Coupling Constants Computed for the d1-d5 Dinuclear Models and for the Crystal Structures of **1** (aAFM) and **2** (sAFM), Along with the Experimental Values

	Cu(pyz)(NO$_3$)$_2$ (**1**)		[Cu(pyz)$_2$(NO$_3$)]NO$_3$·H$_2$O (**2**)	
	Cu···Cu / Å	J / cm^{-1}	Cu···Cu / Å	J / cm^{-1}
d1	6.70	–7.66	6.85	–5.54
d2	5.12	0.12	6.80	–0.12
d3	6.71	–0.08	9.43	–0.02
d4	8.43	0.04	9.66	0.00
d5	8.44	0.00	12.05	0.00
Periodic-DFT		–7.44		–5.59
Exptl.		–7.3		–5.1

Magnetic Coupling Constants. Five possible interaction pathways between two Cu(II) centers have been identified in **1** and **2**, see Figure 2 and Supporting Information. Interactions of type d1 form infinite one-dimensional chains (two of them are present in compound **2**, thus producing a bi-dimensional network). The metallic centers are thus connected by the linearly bridging pyrazine ligands. Instead, interactions of type d2 establish interchain contacts in **1** along the *b* crystallographic direction, whereas d2 in **2** corresponds to the direction of coordination Cu–nitrate. The remaining interactions d3-d5 are longer range contacts connecting two Cu–pyrazine chains. The DFT calculations of the exchange-coupling constants for these dinuclear models afforded the values shown in Table 5, in perfect agreement with a previous calculation.[38] It follows that the experimentally observed magnetic behaviour in **1** and **2**, antiferromagnet with nearest-neighbour exchange constant *J* equals to –7.3 cm^{-1} and –5.1 cm^{-1}, respectively, can be almost exclusively attributed to interactions of type d1. Therefore, for practical purposes, material **1** can be regarded as a quasi-1D spin-1/2 quantum magnet, whereas **2** can be considered a quasi-2D magnet.

These findings are confirmed by periodic calculations on the FM and AFM phases. The unit cells corresponding to the aAFM phase of **1** and the sAFM phase of **2** (Figure 3), thus considering the spin coupling among two Cu centers to be mediated by the pyrazine ligands, are the most stable among the considered systems. When these unit cells are used in conjunction with the corresponding FM cells for estimation of the low-spin-high-spin energy gap, a remarkably good agreement is observed with the experimental exchange-coupling constants (Table 5). Although long-range magnetic ordering has been demonstrated for Cu(pyz)(NO$_3$)$_2$,[14b] the estimated interchain coupling constant, *J'* = +0.03 cm^{-1}, is very small.

Molecular Orbital Analysis and Magnetic Exchange Mechanism. It is now convenient to look at the molecular orbitals relevant to describe the electronic states involved in the magnetic phenomena. Because the exchange-coupling constants are related to the energy difference between states with different spin multiplicities, we focus on the orbitals bearing the unpaired electrons in the low- and high-spin states. We investigated the dinuclear model 1-d1 extracted from the infinite Cu(pyz)(NO$_3$)$_2$ chain that is composed of two metallic centers, each coordinated to two nitrates and two pyrazine ligands. In an unrestricted Kohn-Sham calculation, four molecular orbitals are required for describing the magnetism of the Cu(II) dinuclear model. We adopted the nomenclature proposed by Desplanches and co-workers:[3b] the singly occupied spin-orbitals from the unrestricted calculation are called the occupied magnetic spin-orbitals (OMSOs). For the triplet state of the 1-d1 dinuclear complex, there are two OMSOs and two unoccupied magnetic spin-orbitals (UMSOs), see Supporting Information. Noteworthy, the pyrazine ligand and the O1 atom of the nitrate contribute significantly to the OMSOs, which are of type $d_{x^2-y^2}$ at the metallic center, whereas O2, the oxygen atom weakly coordinated to the Cu, has a negligible contribution to these orbitals. On the other hand, the UMSOs are much more localized at the pyrazine ligands than on the nitrates. At the Cu, the UMSOs clearly present major contributions from the d_{xy} and d_{yz} atomic orbitals. The fact that both occupied and unoccupied magnetic orbitals show large contribution at the pyrazine ligands, and to a less extent at the O1 atom, confirms the role of this ligand as mediator of the Cu···Cu superexchange.

Influence of pyrazine tilt-angle. Exchange through heterocyclic diamines was first verified by Hatfield in a series of Cu(II) 1D polymers.[32a,39] Since then, many studies confirmed that the superexchange occurs mainly along the Cu–diamine–Cu chains.[13,14] In 1976, Hatfield proposed a π-heterocyclic exchange mechanism: the spin coupling would result from the overlap between a π orbital at N and the $3d_{yz}$or $3d_{xy}$ orbital of Cu. If this hypothesis was correct, the superexchange strength should be proportional to the tilt angle of the pyrazine ring relative to the plane defined by the $d_{x^2-y^2}$ magnetic orbital, with a maximum value at 45°. However, in light of more recent crystal structures and magnetic measurements, it seems clear that the tilt angle does not correlate with *J*. Alternatively, a σ-mechanism was proposed,[40] implying that the tilt angle has no influence on the coupling constant. Noteworthy, if at least a small overlap between the Cu d_{yz} or d_{xy} orbital and the pyrazine π molecular orbital would occur, then the π mechanism would also be active, in addition to the σ-exchange.[41]

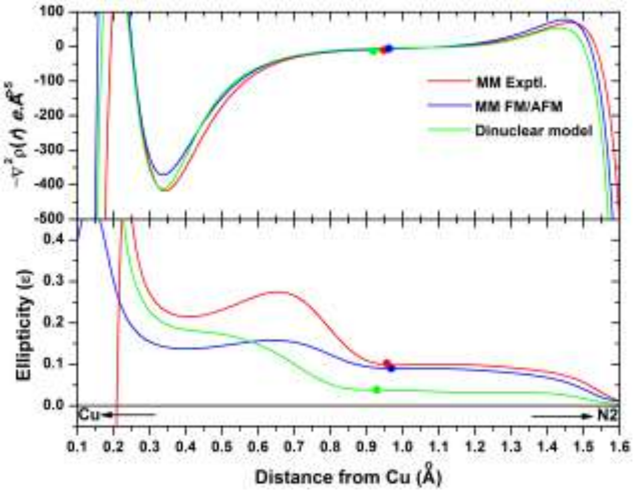

Figure 6. Laplacian and bond ellipticity profiles along the Cu–pyrazine bond-path of Cu(pyz)(NO$_3$)$_2$ (**1**). Filled circles represent the bond critical point positions.

The OMSOs of the 1-d1 dinuclear model show significant σ-overlap along the Cu–pyz bond direction, which could be traced back as the superposition of the $d_{x^2-y^2}$ orbital of Cu with the sp^2-hybridized orbitals at N. Conversely, only the UMSOs are characterized by a π-overlap between both d_{yz} and d_{xy} orbitals of Cu and the p_z orbitals at the pyrazine atoms. Nevertheless, the tilt angle in **1** is 51°, very close to the 45° angle that maximizes the π-overlap. Similarly, in **2**, the tilt angle of the two pyrazine ligands with respect to the $d_{x^2-y^2}$ orbital plane is 53° and 56°.

In order to evaluate the role of N π density in the Cu–N2 bond, a useful parameter is the bond ellipticity (ϵ), which informs on asymmetric concentration of electron density in directions perpendicular to the bond paths. ϵ can be calculated at the bond critical point (see Table 3), but its evaluation along the bond paths provides more significant information.[42] Figure 6 shows the ellipticity profiles of the Cu–N2 coordinative bond in the valence shell region of **1**. The ellipticity reaches a local maximum close to the bond critical point. In the direction BCP–Cu, it decreases only slightly before a large jump caused by the unbalanced d-occupancy. In the direction BCP–pyrazine, instead, the ellipticity drops indicating low preferential accumulation of electronic charge perpendicularly to the bond path. While the theoretical results are biased by the lack of configuration interaction, the experimental result clearly indicates negligible π bonding interaction between Cu and pyrazine.

In view of these results, it seems that the exchange mechanism driven by the π-overlap between the d_{yz} and d_{xy} orbitals of Cu and the p_z orbitals at the pyrazine can be definitely ruled out, in favour of the mechanism based on σ-exchange only.

Spin Density Distributions. The most relevant calculated atomic spin populations are in Table 6 while the spin density distribution for the broken-symmetry singlet state of the dinuclear models 1-d1 and 2-d1 are shown in Figure 7. The spin populations in both compounds are very similar. Although the largest part of the spin density is located at the copper atoms, there is an important delocalization of the unpaired electron, mostly to the N2 donor atoms of the pyrazine ligands, but also to O1 of the nitrate ligand in compound **1**. The minute participation of the O2 in the OMSOs of 1-d1 is appreciated in its rather small negative spin population.

Table 6. Calculated Spin Populations for the Dinuclear Models 1-d1 and 2-d1, and for the Most Stable Phases of **1** (aAFM) and **2** (sAFM)

	Compound **1**		Compound **2**	
	1-d1	aAFM	2-d1	sAFM
Cu	0.649	0.624	0.696	0.652
O1	0.101	0.095	0.001	0.001
O2	–0.003	–0.002	–0.001	0.000
O3	0.011	0.005		
N1	–0.003	–0.004	–0.002	0.000
nitrate	0.106	0.094	–0.003	0.001
C1	–0.003	–0.015	–0.004	0.000
C2			0.006	0.011
C3			0.006	0.014
C4			–0.006	–0.015
N2	0.071	0.102	0.082	0.093
N3			0.077	0.090
pyrazine	0.138	0.148	0.164	0.190

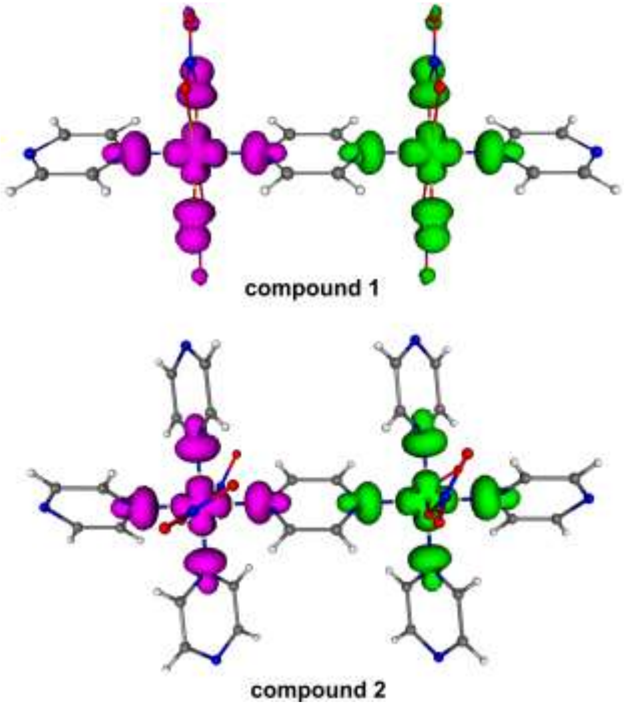

Figure 7. Spin density distributions of the d1 models for **1** and **2** in the broken-symmetry singlet state, represented at an isodensity value of 0.003 au.

The spin density distribution features observed in Table 6 and in Figure 7 can be rationalized in terms of two mechanisms, which explain how the unpaired 3d electron of the Cu places some spin density at the other atoms of the molecule.[6a] On one hand, the molecular orbital that hosts the unpaired electron density, even with major contribution from the $d_{x^2-y^2}$ orbital of the copper center, presents expressive contributions from the ligands, mostly from the N2 donor atoms. If one adopts the convention that the unpaired electron has a positive spin, its delocalization results in a distribution of positive spin density throughout the whole system, as determined by the composition of the OMSOs. This behaviour characterizes the so-called spin delocalization mechanism. On the other hand, the positive spin at the paramagnetic center may induce some spin density of opposite sign at the atoms bonded to it, through a spin polarization mechanism. This results from the exchange term introduced by the Pauli principle, which disfavours the probability of finding two electrons of identical spin in the same region of space. Therefore, the spin of a bonding electron pair is polarized, in such a way that the positive spin is concentrated close to the paramagnetic center, whereas a concentration of negative spin is favoured around the atoms bonded to it. Because this effect also propagates through the system away from the metallic center, the net spin density at a particular atom, resulting from the combination of the two mechanisms, can be either positive or negative. Table 6 shows that the spin delocalization mechanism dominates most of the atomic spin populations, remarkably in the xy plane defined by the Cu–O1 and Cu–N2 bonds, in **1**, and by only Cu–N2 bonds in **2**. However, spin polarization is predominant in the region of the atoms N1, O2 and C1 for compound **1**, and in the atoms N1, C1 and C4 for compound **2**.

Magnetic properties: *T*- and *H*-dependent magnetization. For the sake of comparison to **2**, we remeasured the magnetization of **1** (Figure 8). Broad maxima in $\chi(T)$ are indicative of short-range spin correlations and occur at temperatures of 6.6 and 7.2 K for **1** and **2**, respectively. Of significance in the data for **2** is a subtle kink at 2.6 K, a feature typical of $[Cu(pyz)_2]^{2+}$ square lattices that signals the onset of long-range AFM order.[43] Curie-Weiss analyses of the $\chi(T)$ data for **1** and **2** over the range of $50 \leq T \leq 300$ K yielded the respective Landé-*g* factors of 2.16(1) and 2.11(1) and Weiss constants $\theta = -4.2(3)$ and -4.4(2) K. The negative θ-values indicate antiferromagnetic interactions between $S = 1/2$ Cu(II) ions as mediated by the pyrazine bridges. Further modeling of **1** after a uniform $S = 1/2$ Heisenberg chain gave $g = 2.18$ and $J = 10.5(1)$ K = 7.3 cm^{-1} which agrees with reported values.[14a]

Considering the crystal structure of **2** and most plausible exchange pathways mediated by Cu-pyz-Cu, the $\chi(T)$ data have been fitted to a Heisenberg model for $S = 1/2$ moments arranged on a square-lattice with nearest neighbor antiferromagnetic exchange interactions J, and an isotropic *g*-factor.[44] The resultant fit yields $g = 2.16(1)$ and $J = 7.04(1)$ K = 4.9 cm^{-1}. If the value of $k_B T_N / J = 0.36$ is attributed entirely to finite interplane exchange interactions between Cu(II) ions ($J_\perp$), then Quantum-Monte-Carlo simulations predict the spatial exchange anisotropy to be $|J_\perp / J| = 0.02$.[45] The weak $J_\perp$ is attributed to both the poor donor ability of the NO_3^- ligand and the fact that the long O–Cu–O axis contains the spin-paired d_{z^2} orbital.

For $S = 1/2$ Cu(II) systems with four (magnetically) equivalent bonds to coplanar ions as in **2** and magnetic exchange to neighboring ions in two adjacent planes via NO_3^- bridges, the saturation field (B_{sat}) is given by:[23] $g\mu_B\mu_0 B_{sat} = 4J + 2J_\perp$.

Combining the powder average *g*-factor with the intraplane exchange J deduced from $\chi(T)$, and using the result $|J_\perp / J| << 1$, the critical field is expected at approximately $\mu_0 B_{sat} \geq 21.4$ T. In powdered systems, this B_{sat} may be broadened owing to a spin-orbit coupling correction which results in a *g*-factor anisotropy of the Cu(II) ions.[4] The structure suggests two principle directions for the *g*-factor, corresponding to fields parallel and perpendicular to the $[Cu(pyz)_2]^{2+}$ sheets (the xy and z directions respectively). Typically, an anisotropy of $(g_z - g_{xy})/g_{xy} \approx 10$ % is expected.[1]

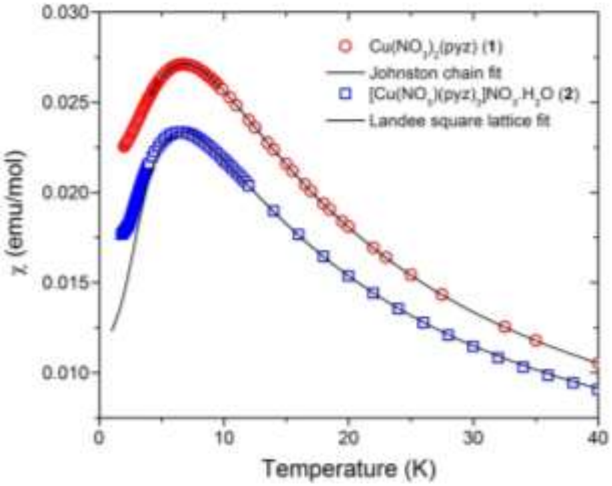

Figure 8. Magnetic susceptibility data for powder samples of **1** and **2** taken in $H_{dc} = 0.1$ T. Solid lines superimposing the data are the result of theoretical fits to Heisenberg 1D and 2D models as described in the text.

The pulsed-field magnetization (M) and associated differential susceptibility (dM/dH) are shown in Figure 9. The predicted critical field falls in-between two features of the differential susceptibility at $\mu_0 H_{c1} = 19.5(5)$ T and $\mu_0 H_{c2} = 23.0(5)$ T. The ratio $H_{c2}/H_{c1} = 1.17(6)$, implies that this broadening of the saturation field is attributed to the *g*-factor anisotropy.

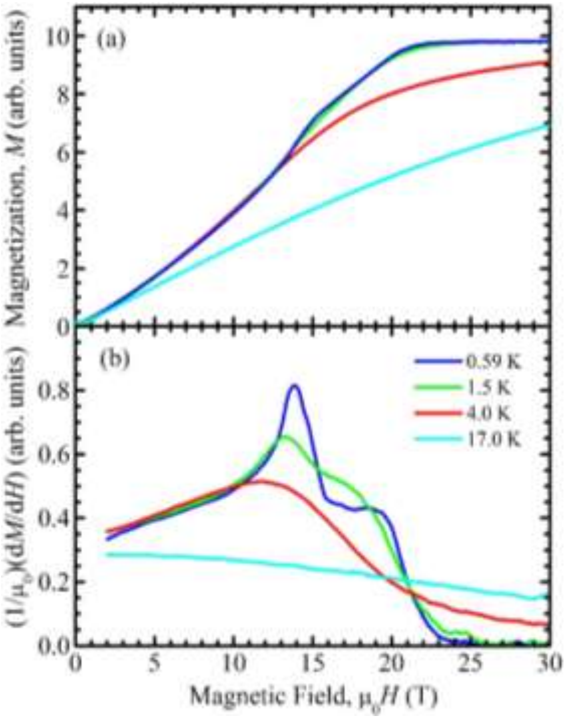

Figure 9. Pulsed-field magnetization and differential susceptibility for $[Cu(NO_3)(pyz)_2]NO_3 \cdot H_2O$ (**2**) obtained at several temperatures above and below the Néel temperature of 2.6 K.

Within this model, the Cu(II) moments first reach the fully aligned ferromagnetic phase for a field applied perpendicular to the $[Cu(pyz)_2]^{2+}$ planes at $H = H_{c1}$. For a powdered sample, this causes dM/dH to decrease since the magnetic response at higher fields will only come from the reduced portion of the sample that remains unsaturated. All of the Cu(II) moments become parallel to the field upon reaching H_{c2}. Using $H_{c2}/H_{c1} = g_z/g_{xy}$ and the powder-average g-factor from the susceptibility, where $g = \sqrt{\frac{g_z^2+2g_{xy}^2}{3}}$, we can extract g_{xy} = 1.99(5) and g_z = 2.32(7). Within the experimental error, these fall within typical values for Cu(II) in octahedral environments.

The pulsed-field magnetization also exhibits a sharp peak in dM/dH at approximately 14 T, resembling a spin-flop feature. This is too low in field to be associated with the saturation field via a g-factor anisotropy, and suggests that there may be other anisotropic terms in the Hamiltonian. A spin-flop is expected for Cu(II) systems with spin-exchange anisotropy, which is a second-order effect that arises from the spin-orbit coupling known to be present in this material. However, the spin-flop associated with this feature is often on a much lower energy scale than the observed H_{sf},[46,47] so the origin of the spin-flop remains unknown.

Long-range magnetic order in 2. Example μ^+SR spectra are plotted in Figure 10. Below T = 2.6 K spontaneous oscillations in $A(t)$ were observed, which are characteristic of the presence of quasi-static long-range magnetic order (LRO). The local magnetic field that results from LRO causes those muons with spin perpendicular to the local field to precess coherently at frequency ν_i, where ν_i is proportional to the magnitude of the local field B. Above 2.6 K, the oscillations vanish and the asymmetry $A(t)$ relaxes following a Gaussian function [$A(t) \propto e^{-\sigma^2 t^2}$].

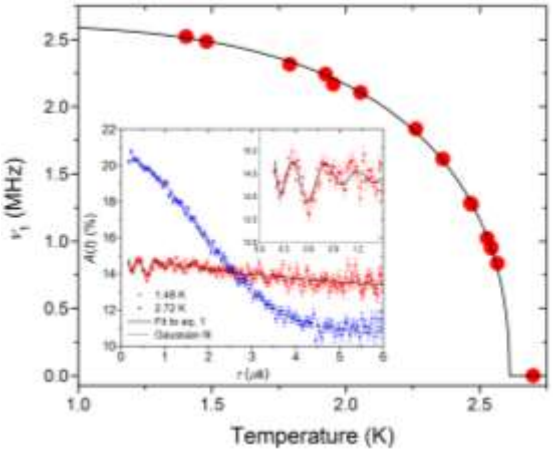

Figure 10. μ^+SR data for **2**: (Main panel) order parameter plot and power law fit used to extract T_N. (Inset) sample μ^+SR spectra measured at T = 1.48 and 2.72 K. Solids lines are fits to the data using eq. 1. Asymmetry spectra for T = 1.48 K at early times better showing the oscillation.

Below 2.6 K, the asymmetry $A(t)$ was fitted to a sum of four oscillatory and one exponential decay component:

$$A(t) = A_{\text{rel}}\big[p_1\cos(2\pi\nu_1 t)e^{-\lambda_1 t} + p_2\cos(2\pi\nu_2 t)e^{-\lambda_2 t} + p_3\cos(2\pi\nu_3 t)e^{-\lambda_3 t} + p_4\cos(2\pi\nu_4 t)e^{-\lambda_4 t} + p_5 e^{-\lambda_5 t}\big] + A_{\text{bg}} \tag{1}$$

where A_{rel} is the total relaxing amplitude, p_i (i = 1,…,5) are the relative fractions for the oscillatory/non-oscillatory components. The parameters ν_i and λ_i are the respective precession frequencies and relaxing rates and A_{bg} accounts for the relaxing contribution from the muons that stop at the sample holder/cryostat tail and muons with a spin component parallel to the local magnetic field. For the fits, the four frequencies were fixed in the proportions $\nu_1 : \nu_2 : \nu_3 : \nu_4$ = 1 : 0.75 : 0.4 : 0.22 throughout the fitting procedure. The relaxing amplitude A_{rel} was fixed at 9.7% and p_i (i = 1,…,5) were fixed at 0.128, 0.112, 0.456, 0.041 and 0.263, respectively. The values of fitted ν_1 are plotted against temperature in the main plot of Figure 10.

The temperature-dependence of the precession frequency was then fitted to the phenomenological function: $\nu_i(T) = \nu_i(0)\left[1-\left(\frac{T}{T_N}\right)^{\alpha}\right]^{\beta}$. The fit yielded T_N = 2.61(1) K, α = 3.96(4) and β = 0.44(4). While the J observed for **2** is less than that for **1**, the higher T_N in **2** is attributed to increased spin dimensionality and the added possibility of spin-exchange anisotropy. This phenomenon is known to be important in describing key magnetic features in the related Cu(II) square lattice Cu(ClO$_4$)$_2$(pyz)$_2$.[43,46]

CONCLUSIONS

In the present work, the electron density distributions of two low-dimensional quantum magnets, Cu(pyz)(NO$_3$)$_2$ and the previously unknown [Cu(NO$_3$)(pyz)$_2$]NO$_3$·H$_2$O, have been determined from a combination of high-resolution single-crystal X-ray diffraction and DFT calculations. The magnetic properties have been correlated with the topological and the integrated properties of the electronic distributions, using the QTAIM partitioning scheme. This has enabled the detailed rationalization of the experimental antiferromagnetic exchange-coupling constants in terms of the intrachain Cu···Cu superexchange interactions. Molecular orbitals and spin density analyses revealed that the spin delocalization through the non-innocent ligand (pyrazine) dominates. Moreover, the experimental electron density unequivocally confirmed that the exchange occurs only through σ-exchange.[41] The spin density concentrates mainly on the atoms directly interacting with the magnetic orbital. However, although the ligand atoms coordinated along the *pseudo*-Jahn-Teller distortion direction bear negligible spin population, the distinctive curvature of the Cu-O2 bond paths and the atomic graph of Cu highlights a small interaction with the magnetic orbital. This feature may deserve more attention investigating other materials of the same kind.

The combination of calculations on the entire crystal and on selected dimers, enabled addressing the gap between stronger exchange interactions (responsible of the dominant features in the magnetic measurements) and weaker interchain couplings.

We are presently investigating a larger series of transition-metal polymeric compounds in order to examine the influence of ligand type and metal nature on the magnetic properties, as well as to identify rigorous signature of magnetic interactions in the electron density distributions.[48] In a long term view, we expect to develop empirical or semi-empirical methodologies to predict the magnetic susceptibilities, based on the electron density distributions of the materials building blocks, similarly to what done for the electric susceptibilities.[49]

ASSOCIATED CONTENT

Supporting Information. Details of X-ray diffraction and magnetic measurements, electron density refinements and DFT calculations. This material is available free of charge via the Internet at http://pubs.acs.org.

AUTHOR INFORMATION

Corresponding Author

(JLM) jmanson@ewu.edu
(PM) piero.macchi@dcb.unibe.ch

Funding Sources

The Swiss National Science Foundation (SNF-141271 and 160157) and the US National Science Foundation (DMR-1306158).

ACKNOWLEDGMENT

Part of this work was carried out at the STFC ISIS Facility, Rutherford-Appleton Laboratory UK. We thank the EPSRC (UK) and the John Templeton Foundation for financial support and appreciate the experimental assistance provided by A. Vaidya. Work performed at the National High Magnetic Field Laboratory, USA, was supported by the National Science Foundation Cooperative Agreement No. DMR-1157490, the State of Florida, and the U.S. Department of Energy (DoE) and through the DoE Basic Energy Science Field Work Proposal “Science in 100 T.”

REFERENCES

(1) (a) Getzlaff, M. *Fundamentals of Magnetism;* Springer: Berlin, 2008. (b) Gatteschi, D.; Sessoli, R.; Villain, J. *Molecular Nanomagnets;* Oxford University Press: New York, 2006. (c) Miller, J. S.; Drillon, M. (Eds.) *Magnetism: Molecules to Materials I-V;* VCH: New York, 2001.

(2) (a) Hoffert, W. A.; Rappé, A. K.; Shores, M. P. *J. Am. Chem. Soc.* **2011**, *133*, 20823-20836. (b) Atanasov, M.; Delley, B.; Neese, F.; Tregenna-Piggott, P. L.; Sigrist, M. *Inorg. Chem.* **2011**, *50*, 2112-2124. (c) Manson, J. L.; Schlueter, J. A.; Funk, K. A.; Southerland, H. I.; Twamley, B.; Lancaster, T.; Blundell, S. J.; Baker, P. J.; Pratt, F. L.; Singleton, J.; McDonald, R. D.; Goddard, P. A.; Sengupta, P.; Batista, C. D.; Ding, L.; Lee, C.; Whangbo, M.-H.; Franke, I.; Cox, S.; Baines, C.; Trial, D. *J. Am. Chem. Soc.* **2009**, *131*, 6733-6747.

(3) (a) Cauchy, T.; Ruiz, E.; Jeannin, O.; Nomura, M.; Fourmigué, M. *Chem. Eur. J.* **2007**, *13*, 8858-8866. (b) Desplanches, C.; Ruiz, E.; Rodrígues-Fortea, A.; Alvarez, S. *J. Am. Chem. Soc.* **2002**, *124*, 5197-5205. (c) Manson, J. L.; Conner, M. M.; Schlueter, J. A.; McConnell, A. C.; Southerland, H. I.; Pratt, F. L.; Singleton, J.; McDonald, R. D.; Lee, C.; Whangbo, M.-H. *Chem. Mater.* **2008**, *20*, 7408-7416.

(4) Kahn, O. *Molecular Magnetism;* VCH: New York, 1993.

(5) (a) Fabrizi de Biani, F.; Ruiz, E.; Cano, J.; Novoa, J. J.; Alvarez, S. *Inorg. Chem.* **2000**, *39*, 3221-3229. (b) Cano, J.; Ruiz, E.; Alvarez, S.; Verdaguer, M. *Comments Inorg. Chem.* **1998**, *20*, 27-56.

(6) (a) Ruiz, E.; Cirera, J.; Alvarez, S. *Coord. Chem. Rev.* **2005**, *249*, 2649-2660. (b) Gillon, B. In *Magnetism: Molecules to Materials I;* Miller, J. S.; Drillon, M. (Eds.); VCH: New York, 2001. pp 357-378.

(7) Schweizer, J. In *Neutron Scattering from Magnetic Materials;* Chatterji, T., (Ed.); Elsevier: Amsterdam, 2006. pp 153-213.

(8) Deutsch, M.; Claiser, N.; Pillet, S.; Chumakov, Y.; Becker, P.; Gillet, J.-M.; Lecomte, C.; Souhassou, M. *Acta Crystallogr., Sect. A* **2012**, *68*, 675-686.

(9) (a) Ruiz, E.; Alvarez, S.; Rodrígues-Fortea, A.; Alemany, P.; Pouillon, Y.; Massobrio, C. In *Magnetism: Molecules to Materials II;* Miller, J. S.; Drillon, M. (Eds.); VCH: New York, 2003. pp 227-279. (b) Poblet, J. M.; López, X.; Bo, C. *Chem. Soc. Rev.* **2003**, *32*, 297-308.

(10) Ruiz, E. *Struct. Bond.* **2004**, *113*, 71-102.

(11) (a) Overgaard, J.; Walsh, J. P.; Hathwar, V. R.; Jørgensen, M. R. V.; Hoffman, C.; Platts, J. A.; Piltz, R.; Winpenny, R. E. P. *Inorg. Chem.* **2014**, *53*, 11531-11539. (b) Pillet, S.; Souhassou, M.; Lecomte, C. *Acta Crystallogr., Sect. A* **2004**, *60*, 455-464. (c) Pillet, S.; Souhassou, M.; Mathonière, C.; Lecomte, C. *J. Am. Chem. Soc.* **2004**, *126*, 1219-1228. (d) Overgaard, J.; Hibbs, D. E.; Rentschler, E.; Timco, G. A.; Larsen, F. K. *Inorg. Chem.* **2003**, *42*, 7593-7601.

(12) (a) Manson, J. L.; Baldwin, A. G.; Scott, B. L.; Bendix, B. L.; Del Sesto, R. E.; Goddard, P. A.; Kohama, Y.; Tran, H. E.; Ghannadzadeh, S.; Singleton, J.; Lancaster, T.; Möller, J. S.; Blundell, S. J.; Pratt, F. L.; Zapf, V. S.; Kang, J.; Lee, C.; Whangbo, M.-H.; Baines, C. *Inorg. Chem.* **2012**, *51*, 7520-7528. (b) Amo-Ochoa, P.; Delgado, E.; Gómez-García, C. J.; Hernández, D.; Hernández, E.; Martin, A.; Zamora, F. *Inorg. Chem.* **2013**, *52*, 5943-5950.

(13) (a) Amo-Ochoa, P.; Castillo, O.; Gómez-García, C. J.; Hassanein, K.; Verma, S.; Kumar, J.; Zamora, F. *Inorg. Chem.* **2013**, *52*, 11428-11437. (b) Herringer, S. N.; Deumal, M.; Ribas-Arino, J.; Novoa, J. J.; Landee, C. P.; Wikara, J. L.; Turnbull, M. M. *Chem. Eur. J.* **2014**, *20*, 8355-8362.

(14) (a) Hammar, P. R.; Stone, M. B.; Reich, D. H.; Broholm, C.; Oshikawa, M. *Phys. Rev. B* **1999**, *59*, 1008-1015. (b) Lancaster, T.; Blundell, S. J.; Brooks, M. L.; Baker, P. J.; Pratt, F. L.; Manson, J. L.; Landee, C. P.; Baines, C. *Phys. Rev. B* **2006**, *73*, 020410.

(15) Agilent Technologies. *CrysAlisPro*. Version 1.171.37.31 (release 14-01.2014 CrysAlis171.NET). Yarnton, UK. 2014.

(16) Blessing, R. H. *Crystallogr. Rev.* **1987**, *1*, 3-58.

(17) Sheldrick, G. M. *Acta Cystallogr., Sect. A* **2008**, *64*, 112-122.

(18) Volkov, A.; Macchi, P.; Farrugia, L. J.; Gatti, C.; Mallinson, P.; Richter, T.; Koritsanszky, T. XD2006 – A Computer Program Package for Multipole Refinement , Topological Analysis of Charge Densities and Evaluation of Intermolecular Interaction Energies from Experimental and Theoretical Structure Factors. University at Buffalo, State University of New York, NY, USA; University of Milano, Italy; University of Glasgow, UK; CNRISTM, Milano, Italy; Middle Tennessee State University, TN, USA. 2006.

(19) Becker, P. J.; Coppens, P. *Acta Crystallogr., Sect. A* **1974**, *30*, 129-147.

(20) Farrugia, L. J.; Mallinson, P. R.; Stewart, B. *Acta Crystallogr., Sect. B* **2003**, *59*, 234-247.

(21) Herbst-Irmer, R.; Henn, J.; Holstein, J. J.; Hübschle, C. B.; Dittrich, B.; Stern, D.; Kratzert, D.; Stalke, D. *J. Phys. Chem. A* **2012**, *117*, 633-641.

(22) Kamiński, R.; Domagała, S.; Jarzembska, K. N.; Hoser, A. A.; Sanjuan-Szklarz, F.; Gutmann, M. J.; Makal, A.; Malińska, M.; Bąk, J. M.; Woźniak, K. *Acta Crystallogr., Sect. A* **2014**, *70*, 72-91.

(23) Goddard, P. A.; Singleton, J.; Sengupta, P.; McDonald, R. D.; Lancaster, T.; Blundell, S. J.; Pratt, F. L.; Cox, S.; Harrison, N.; Manson, J. L.; Southerland, H. I.; Schlueter, J. A. *New J. Phys*. **2008**, *10*, 083025.

(24) (a) Noodleman, L. *J. Chem. Phys.* **1981**, *74*, 5737-5743. (b) Noodleman, L.; Davidson, E. R. *Chem. Phys.* **1986**, *109*, 131-143. (c) Deumal, M.; Bearpark, M. J.; Novoa, J. J.; Robb, M. A. *J. Phys. Chem. A* **2002**, *106*, 1299-1315. (d) Ruiz, E.; Cano, J.; Alvarez, S.; Alemany, P. *J. Comput. Chem.* **1999**, *20*, 1391-1400.

(25) Frisch, M. J.; Trucks, G. W.; Schlegel, H. B.; Scuseria, G. E.; Robb, M. A.; Cheeseman, J. R.; Scalmani, G.; Barone, V.; Mennucci, B.; Petersson, G. A.; Nakatsuji, H.; Caricato, M.; Li, X.; Hratchian, H. P.; Izmaylov, A. F.; Bloino, J.; Zheng, G.; Sonnenberg, J. L.; Hada, M.; Ehara, M.; Toyota, K.; Fukuda, R.; Hasegawa, J.; Ishida, M.; Nakajima, T.; Honda, Y.; Kitao, O.; Nakai, H.; Vreven, T.; Montgomery, J. A., Jr.; Peralta, J. E.; Ogliaro, F.; Bearpark, M.; Heyd, J. J.; Brothers, E.; Kudin, K. N.; Staroverov, V. N.; Kobayashi, R.; Normand, J.; Raghavachari, K.; Rendell, A.; Burant, J. C.; Iyengar, S. S.; Tomasi, J.; Cossi, M.; Rega, N.; Millam, J. M.; Klene, M.; Knox, J. E.; Cross, J. B.; Bakken, V.; Adamo, C.; Jaramillo, J.; Gomperts, R.; Stratmann, R. E.; Yazyev, O.; Austin, A. J.; Cammi, R.; Pomelli, C.; Ochterski, J. W.; Martin, R. L.; Morokuma, K.; Zakrzewski, V. G.; Voth, G. A.; Salvador, P.; Dannenberg, J. J.; Dapprich, S.; Daniels, A. D.; Farkas, Ö.; Foresman, J. B.; Ortiz, J. V.; Cioslowski, J.; Fox, D. J. Gaussian 09; Gaussian, Inc.: Wallingford, CT, 2009.

(26) Keith, T. A. AIMAll, Version 14.04.17; TK Gristmill Software: Overland Park, KS, USA, 2014, aim.tkgristmill.com.

(27) Dovesi, R.; Saunders, V. R.; Roetti, C.; Orlando, R.; Zicovich-Wilson, C. M.; Pascale, F.; Civalleri, B.; Doll, K.; Harrison, N. M.; Bush, I. J.; D'Arco, P.; Llunell, M. *CRYSTAL09 User's Manual.* Torino: University of Torino, 2009.

(28) Doll, K.; Harrison, N. M. *Chem. Phys. Lett.* **2000**, *317*, 282-289.

(29) Gatti, C.; Saunders, V. R.; Roetti, C. *J. Chem. Phys.* **1994**, *101*, 10686-10696.

(30) Gatti, C. *TOPOND.* CNR-CSRSRC, Milan, Italy, 2009.

(31) (a) Dovesi, R.; Fava, F. F.; Roetti, C.; Saunders, V. R. *Faraday Discuss.* **1997**, *106*, 173-187. (b) Reinhardt, P.; Moreira, I. de P. R.; de Graaf, C.; Dovesi, R.; Illas, F. *Chem. Phys. Lett.* **2000**, *319*, 625-630. (c) Datta, S. N.; Hansda, S. *Chem. Phys. Lett.* **2015**, *621*, 102-108.

(32) (a) Crawford, V. H.; Richardson, H. W.; Wasson, J. R.; Hodgson, D. J.; Hatfield, W. E. *Inorg. Chem.* **1976**, *15*, 2107-2110. (b) Laborda, S.; Clérac, R.; Anson, C. E.; Powell, A. K. *Inorg. Chem.* **2004**, *43*, 5931-5943. (c) Walsh, J. P. S.; Sproules, S.; Chilton, N. F.; Barra, A.-L.; Timco, G. A.; Collison, D.; McInnes, E. J. L.; Winpenny, R. E. P. *Inorg. Chem.* **2014**, *53*, 8464-8472.

(33) Santoro, A.; Mighell, A. D.; Reimann, C. W. *Acta Crystallogr., Sect. B* **1970**, *26*, 521-526.

(34) (a) Gibbs, G. V.; Downs, R. T.; Cox, D. F.; Rosso, K. M.; Ross, N. L.; Kirfel, A.; Lippmann, T.; Morgenroth, W.; Crawford, T. D. *J. Phys. Chem. A* **2008**, *112*, 8811-8823. (b) Macchi, P.; Sironi, A. *Coord. Chem. Rev.* **2003**, *238*, 383-412.

(35) Mebs, S.; Kalinowski, R.; Grabowsky, S.; Förster, D.; Kickbusch, R.; Justus, E.; Morgenroth, W.; Paulmann, C.; Luger, P.; Gabel, D.; Lentz, D. *Inorg. Chem.* **2011**, *50*, 90-103.

(36) Holladay, A.; Leung, P.; Coppens, P. *Acta Crystallogr., Sect. A* **1983**, *39*, 377-387.

(37) (a) Figgis, B. N.; Lewis, J. In *Modern Coordination Chemistry: Principles and Methods;* Lewis, J.; Wilkins, R. G. (Eds.); Wiley: New York, 1960. pp 400-454. (b) Vulfson, S. G. Molecular Magnetochemistry; Overseas Publishers Association: Amsterdam, 1998.

(38) Jornet-Somoza, J.; Deumal, M.; Robb, M. A.; Landee, C. P.; Turnbull, M. M.; Feyerherm, R.; Novoa, J. J. *Inorg. Chem.* **2010**, *49*, 1750-1760.

(39) Richardson, H. W.; Wasson, J. R.; Hatfield, W. E. *Inorg. Chem.* **1977**, *16*, 484-486.

(40) Mohri, F.; Yoshizawa, K.; Yambe, T.; Ishida, T.; Nogami, T. *Mol. Eng.* **1999**, *8*, 357-373.

(41) Butcher, R. T. *PhD Thesis;* Clark University, Worcester, 2008.

(42) Scherer, W.; Herz, V.; Hauf, C. *Struct. Bond.* **2012**, *146*, 159-204.

(43) (a) Xiao, F.; Woodward, F.; Landee, C. P.; Turnbull, M. M.; Mielke, C.; Harrison, N.; Lancaster, T.; Blundell, S. J.; Baker, P. J.; Babkevich, P.; Pratt, F. L. *Phys. Rev. B* **2009**, *79*, 134412.

(44) Woodward, F. M.; Gibson, P. J.; Jameson, G. B.; Landee, C. P.; Turnbull, M. M.; Willett, R. D. *Inorg. Chem*. **2007**, *46*, 4256-4266.

(45) Yasuda, C.; Todo, S.; Hukushima, K.; Alet, F.; Keller, M.; Troyer, M.; Takayama, H. *Phys. Rev. Lett*. **2005**, *94*, 217201.

(46). Tsyrulin, N.; Xiao, F.; Schneiderwind, A.; Link, P.; Ronnow, H.; Gavilano, J.; Landee, C. P.;Turnbull, M. M.; Kenzelmann, M. *Phys. Rev. B* **2010**, *81*, 134409.

(47). Goddard, P.; Franke, I.; Singleton, J.; Lancaster, T.; Brambleby, J.; Möller, J. S.; Steele, A. J.; Blundell, S. J.; Baines, C.; Topping, C. V.; Modic, K.; McDonald, R. D.; Lapidus, S. H.; Stephens, P. W.; Tramley, B. W.; Funk, K.; Conner, M. M.; Corbey, J. F.; Tran, H. E.; Schlueter, J. A.; Manson, J. L. **2015**, manuscript in preparation.

(48) (a) Scherer, W.; Dunbar, A. C.; Barquera-Lozada, J. E.; Schmitz, D.; Eickerling, G.; Kratzert, D.; Stalke, D.; Lanza, A.; Macchi, P.; Casati, N. P. M.; Ebad-Allah, J.; Kuntscher, C. *Angew. Chem. Int. Ed.* **2015**, *54*, 2505-2509. (b) Lanza, A.; Fiolka, C.; Fisch, M.; Casati, N.; Skoulatos, M.; Rüegg, C.; Krämer, K. W.; Macchi, P. *Chem. Comm.* **2014**, *50*, 14504-14507.

(49) (a) Dos Santos, L. H. R.; Krawczuk, A.; Macchi, P. *J. Phys. Chem. A* **2015**, *119*, 3285-3298. (b) Chimpri, A. S.; Gryl, M.; Dos Santos, L. H. R.; Krawczuk, A.; Macchi, P. *Cryst. Growth Des.* **2013**, *13*, 2995-3010.

Insert Table of Contents artwork here